Supplementary material for "*Flattened and wrinkled encapsulated droplets: Shape-morphing induced by gravity and evaporation*"

Davide Riccobelli,[1] Hedar H. Al-Terke,[2, 3] Päivi Laaksonen,[4] Pierangelo Metrangolo,[5, 2, 3]
Arja Paananen,[6] Robin H. A. Ras,[2, 3] Pasquale Ciarletta,[1] and Dominic Vella[7]

[1] *MOX – Dipartimento di Matematica, Politecnico di Milano, Italy*
[2] *Department of Applied Physics, Aalto University School of Science, Finland*
[3] *Center of Excellence in Life–Inspired Hybrid Materials (LIBER), Aalto University, Finland*
[4] *HAMK Tech, Häme University of Applied Sciences*
[5] *Department of Chemistry, Materials, and Chemical Engineering "Giulio Natta", Politecnico di Milano, Italy*
[6] *VTT Technical Research Centre of Finland Ltd, Finland*
[7] *Mathematical Institute, University of Oxford, Woodstock Rd, Oxford, OX2 6GG, UK.*
(Dated: April 8, 2023)

This Supplementary material contains further details of the experimental procedures used in this work (§I) as well as a dimensional analysis of the relative importance of the various physical effects at work in the experimental problem (§II) and the details of the theoretical model used to predict the interface shape (§III).

I. MATERIALS AND METHODS

A. Droplet preparation

HFBI Hydrophobin protein is produced and purified as described by Linder *et al.* [1] and dispersed in Milli-Q water, which is water purified using a Milli-Q system (Millipore) with resistivity around $18.2\,\mathrm{M\Omega\,cm}$.

A water droplet containing HFBI hydrophobin molecules is placed on a parafilm substrate using a micro-pipette. The droplet is monitored using an optical tensiometer (Biolin Attention Theta Goniometer, Finland) and the profile of the droplet captured using a CCD camera at a frame rate of 0.05 fps. All the experiments are performed at room temperature (around $20\,^\circ\mathrm{C}$) and with a relative humidity of 25%. In the experiments with pendant droplets, a water droplet containing HFBI molecules is placed on the parafilm substrate in the sessile state and the film is quickly inverted to yield the pendant state (see FIG. 1 of the main text).

B. Image processing

Experimental images are processed with several software packages to extract the profile of the evaporating drops. First, the pictures are converted to binary images using IMAGEJ and processed using the library MORPHOLIBJ [2]. The droplet interface is determined by extracting the boundaries using the Python library OPENCV. Finally, the drop profiles obtained in this way are processed using MATHEMATICA to extract information such as the volume of the drop, the diameter of the flat spot of the surface, and the height of the drop. FIG. S1 shows examples of the shape evolution determined in this way.

Time lapse videos of the evolution of droplet shape through evaporation are shown for the sessile and pendant configurations in the movies `SM_video_sessile.avi` and `SM_video_pendant.avi`, respectively. In these movies, images are presented at intervals of 20 s. We observe that the evaporation rate of the droplets is approximately constant in time and is not significantly influenced by the formation of the HFBI membrane, as shown in FIG. S2.

C. Sample preparation for Atomic Force Microscopy (AFM)

A droplet of $100\,\mu\mathrm{L}$ of HFBI solution $(0.2\,\mathrm{g\,L^{-1}})$ was placed on a parafilm substrate for about one hour to get a flattened area on the top of the droplet and to test the assembly of a HFBI monolayer at the interface. After that, a highly ordered pyrolytic graphite (HOPG) substrate was brought into contact with the top of the droplet. By gently washing it with $200\,\mathrm{mL}$ of Milli-Q water the excess HFBI molecules were taken out. The sample was then placed on the AFM stage and, after waiting around $30\,\mathrm{min}$ to ensure the sample was dry, the sample was imaged. The full experimental pipeline is sketched in FIG. S3).
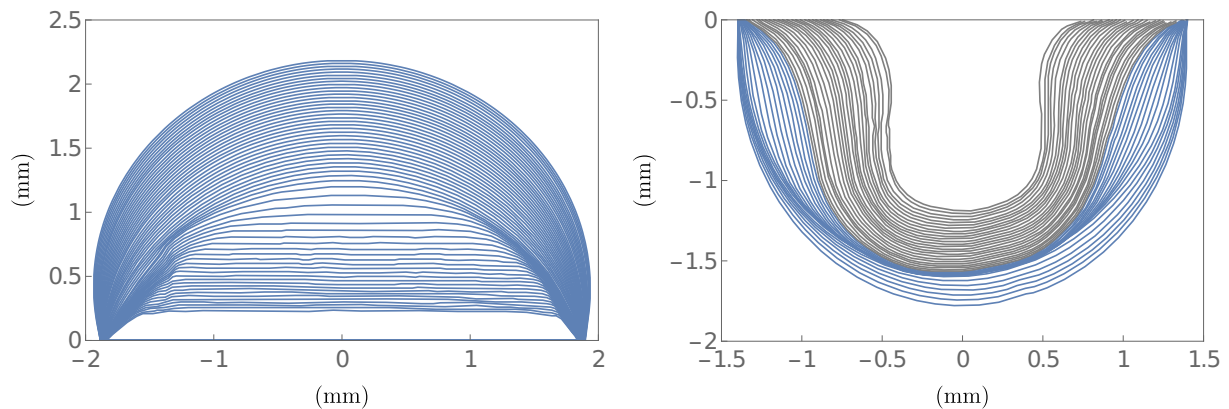
FIG. S1. Plots of the extracted experimental profiles for (left) a sessile droplet with initial volume $V_i = 18.68\,\mathrm{mm}^3$ and initial concentration $C = 2\,\mathrm{\mu mol\,L}^{-1}$ and (right) a pendant droplet with initial volume $V_i = 7.77\,\mathrm{mm}^3$ and initial concentration $C = 4\,\mathrm{\mu mol\,L}^{-1}$. Individual curves show the shape extracted at intervals of one minute from the start of evaporation. We note that the contact line is initially pinned in pendant droplets, but ultimately depins after some level of evaporation. We identified contact line depinning as when the contact radius has diminished by more than 4% from its initial value; we distinguish profiles in which the contact line is depinned by using gray curves (rather than blue curves, which represent the profiles of pinned droplets).
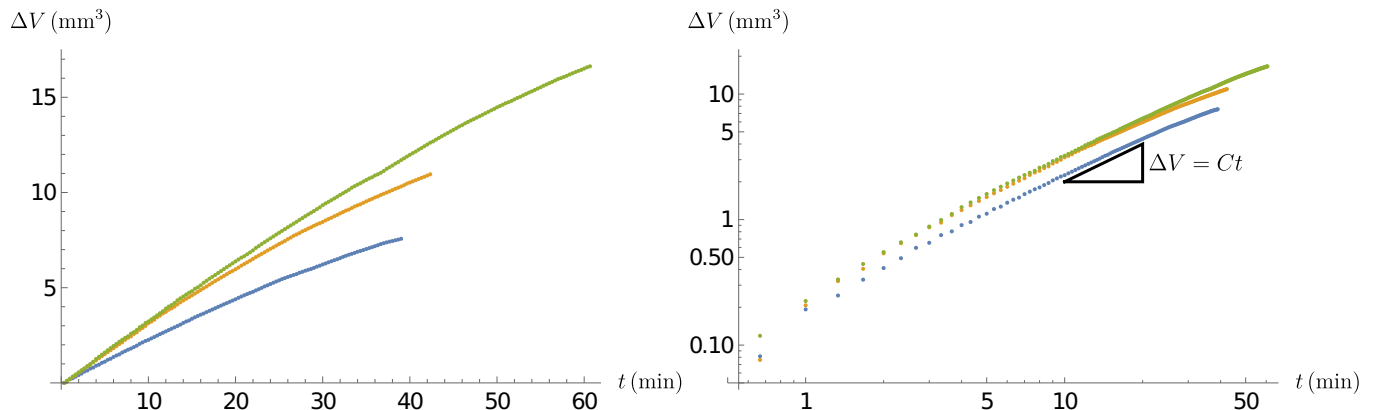

FIG. S2. (Left) Evaporated volume, ΔV, plotted as function of time for three droplets with initial volume $V = 8.63,\ 13.05,\ 18.68\,\mathrm{mm}^3$ (blue, orange, and green dots, respectively) and initial concentration $C = 2\,\mathrm{\mu mol\,L}^{-1}$. (Right) The same data plotted using logarithmic axes. The triangle indicates the slope expected for a linear relation (i.e. a constant evaporation rate).

D. Atomic force microscopy

A Dimension Icon AFM (Bruker AXS, France; formerly Veeco) was used to carry out the atomic force microscopy (AFM) experiments. The device is equipped with a ScanAsyst-air cantilever (sharp silicon nitride tip with a nominal radius of $2\,\mathrm{nm}$ for PeakForce Tapping in air). With a resolution of $256\,\mathrm{pix} \times 256\,\mathrm{pix}$ and scan rate of $1\,\mathrm{kHz}$, the AFM scanning was performed for a $100\,\mathrm{nm} \times 100\,\mathrm{nm}$ scan area. ScanAsyst Auto control was set to "individual" for the sample with PeakForce Amplitude of $170\,\mathrm{nm}$. The spring constant and peak force frequency were $0.4\,\mathrm{N\,m}^{-1}$ and $2\,\mathrm{kHz}$ for all samples. Individual scans for each sample were taken at multiple locations on the surface. An example scan is shown in FIG. S3b.
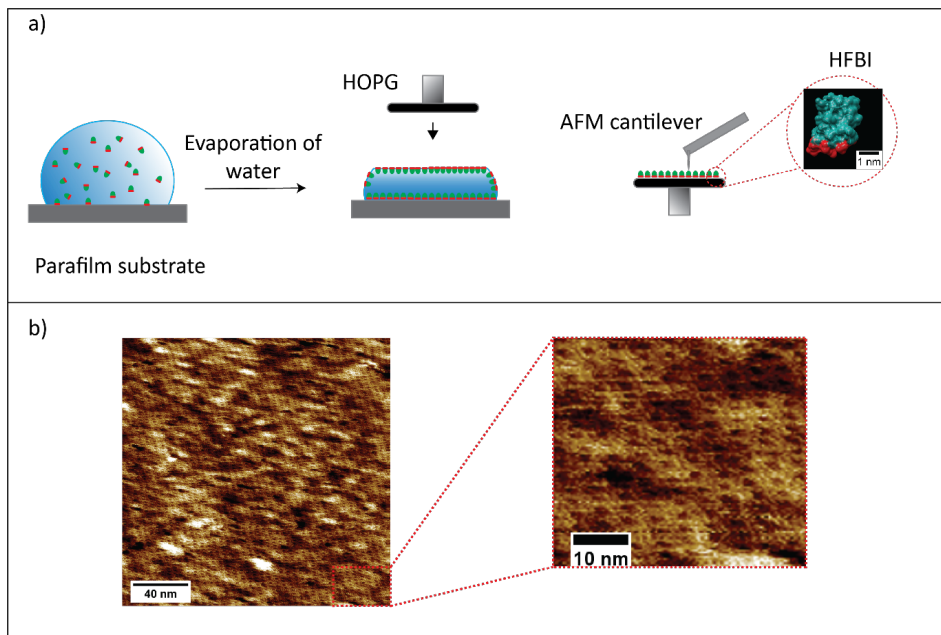
FIG. S3. a) Schematic showing the preparation of the sample for AFM imaging. b) AFM image of a hydrophobin monolayer formed at an air–water interface after being transferred to an HOPG surface.

II. DIMENSIONAL ANALYSIS

A. Dimensional parameters

The fundamental physical parameters of this system, used to develop our model, are collected in Table S1. Other fundamental parameters can be computed as derived quantities for the physics at hand. In particular, the apparent diffusivity D_H of HFBI in water is given by the Stokes–Einstein relation [3]:

$$D_H = \frac{\kappa_B T_0}{6\pi\mu a} = 1.4 \times 10^{-10}\,\mathrm{m^2/s},$$

where $\kappa_B = 1.38 \times 10^{-23}\,\mathrm{m^2\,kg\,s^{-2}\,K^{-1}}$ is the Boltzmann constant. At room temperature, $T_0 \approx 293$ K, the saturated water vapor pressure p_v can be computed as [4]:

$$p_v = 610.78\,\mathrm{Pa}\,\exp\left(\frac{17.26(T_0 - 273.16\,\mathrm{K})}{T_0 - 34.86\,\mathrm{K}}\right) = 2325.98\,\mathrm{Pa},$$

allowing us to compute the vapour saturation concentration c_v as:

$$c_v = 0.002\,166\,\frac{\mathrm{K\,s^2}}{\mathrm{m^2}}\frac{p_v}{T_0} = 1.72 \times 10^{-2}\,\mathrm{kg\,m^{-3}}.$$

B. Characteristic parameters

We start by introducing the main characteristic quantities that enter the model of the system presented in the main paper. We are particularly focused on understanding the forces that are involved in determining the shape of the droplet, since this is the focus of the paper.

C. Gravitational effect on individual molecules

The previous suggestion has been that the effect of gravity on individual molecules is important. Here we estimate the importance of this effect by estimating the sedimentation length, ℓ_s, that is the height over which the gravitational

Parameter	Symbol	Value	REF.
water density	ρ	$1 \times 10^3 \, \mathrm{kg\,m^{-3}}$	[5]
HFBI density	ρ_H	$1.13 \times 10^3 \, \mathrm{kg\,m^{-3}}$	[6]
humidity	h	25%	Measured
surface tension droplet-air	γ	$55 \times 10^{-3} \, \mathrm{N\,m^{-1}}$	[7] (FIG. 22 p.34)
size of HFBI particle	a	$1.5 \, \mathrm{nm}$	[8]
water viscosity	μ	$10^{-3} \, \mathrm{Pa\,s}$	[5]
thermal conductivity water	k_w	$0.58 \, \mathrm{W\,m^{-1}\,K^{-1}}$	[9]
initial room temperature	T_0	$293 \, \mathrm{K}$	Measured
diffusivity of vapor in air	D_w	$26.1 \times 10^{-5} \, \mathrm{m^2\,s^{-1}}$	[10]
latent heat of vaporization	H_v	$2260 \, \mathrm{kJ\,kg^{-1}}$	[11]
coefficient of variation of surface tension	$\beta = d\gamma/dT$	$-0.16 \, \mathrm{mN/K/m}$	[12]

TABLE S1. Physical parameters of the system that are used to develop the model presented here.

potential energy of the molecule would become comparable to the thermal energy, $\kappa_B T$, [13]. For systems that are small compared to ℓ_s, thermal energy is expected to overwhelm the effects of gravity.

The sedimentation length is calculated as

$$\ell_s = \frac{\kappa_B T_0}{\Delta \rho g a^3}$$

where $\Delta \rho = \rho_H - \rho = 130 \, \mathrm{kg\,m^{-3}}$ is the density difference between HFBI and water, g is the acceleration due to gravity and a is the molecular size. We therefore have that $\ell_s \approx 1 \, \mathrm{km}$. As this kilometre length scale is at least five orders of magnitude larger than any relevant length scale in the problem, it is safe to neglect the effect of gravity on individual molecules. Instead, we turn to consider the effect of gravity on the droplet itself.

1. Gravity versus surface tension for the droplet

The shape of a stationary liquid droplet, in equilibrium, is controlled by a balance between surface tension and gravity. This balance introduces a characteristic length scale, the capillary length ℓ_c, which is defined as:

$$\ell_c = \sqrt{\frac{\gamma}{\rho g}} = 2.37 \, \mathrm{mm},$$

where g is the acceleration due to gravity. We note that ℓ_c is of the same order as the contact radius r_c of the droplet and, further, that the Bond number

$$\mathrm{Bo} = \pm \left(\frac{V_i}{\ell_c^3} \right)^{2/3} \approx \pm 1,$$

where the plus or minus sign depends on the orientation of the droplet with respect to gravity. Specifically, we take a positive sign for sessile droplets, while Bo is negative in pendant droplets. Since $|\mathrm{Bo}| \approx 1$, gravity cannot be neglected when computing the shape of the droplet — the effects of the droplet's weight and surface tension are expected to be of similar order.

2. Fluid flow

Having seen that the effects of gravity and capillarity are of the same order of magnitude within the droplet, the question then arises of whether the shape of the droplet is determined by these forces (together with elasticity), or whether the fluid flow induced by evaporation plays an important role.

We begin by estimating the characteristic velocity, v_c, of the capillary flow driven by evaporation: the evaporative flux is driven by steady-state diffusion [14, 15], and hence has magnitude $j \sim D_w c_v / \ell_c$ where we assume that diffusion

occurs over the typical size of the drop (itself comparable to the capillary length) and the typical vapour concentration is c_v. Since this represents a mass flux per unit area (recall that c_v is a mass per volume) it yields a capillary velocity:

$$v_c = \frac{D_w c_v}{\rho \ell_c} \approx 1.89 \, \mu\mathrm{m \, s}^{-1}.$$

The Reynolds number associated with this flow is

$$\mathrm{Re} = \frac{\rho v_c \ell_c}{\mu} \approx 4 \times 10^{-3},$$

so that inertia is negligible in comparison to viscous forces, while the relative importance of viscous to capillary forces is controlled by the capillary number

$$\mathrm{Ca} = \frac{\mu v_c}{\gamma} = 3.4 \times 10^{-8}.$$

This shows that viscous forces are negligible in comparison to capillary forces, and the droplet shape is therefore governed by static considerations, as assumed in the model of the main paper.

3. Temperature change and Marangoni effects

The evaporation of liquid with the flux j, may also induce a temperature change — the rate at which heat energy is lost through evaporation is jH_v with H_v (the latent heat of vaporization), heat that must be supplied by thermal conduction through the droplet driven by a temperature change $\Delta T \sim jH_v/(k_w/\ell_c)$, so that the characteristic temperature ΔT is given by

$$\Delta T = \frac{D_w H_v c_v}{k_w} = 17.51 \, \mathrm{K}.$$

The most important consequence of an evaporation-induced temperature change is its effect on the surface tension coefficient of the droplet — since evaporation occurs preferentially near the contact line of a droplet [14], not uniformly over the surface, the temperature-induced changes in surface tension coefficient would also lead to Marangoni flows, with their associated stresses. (We assume that other sources of Marangoni stress, e.g., surfactant concentration gradients, are negligible [16].) Accordingly $\gamma(T) = \gamma(T_0) + \beta(T - T_0) + O(T - T_0)^2$, and the typical change in γ caused by temperature changes is

$$\mathrm{Ma} = \frac{|\Delta\gamma|}{\gamma} \sim |\beta\Delta T/\gamma| \approx 0.05.$$

Let H be the height of the droplet. Marangoni effects are therefore expected to induce a fluid flow of velocity u_M such that $\mu u_M / H \sim \gamma \mathrm{Ma}/\ell_c$, so that the capillary number associated with the surface tension gradient is:

$$\mathrm{Ca_{Ma}} = \frac{\mu u_M}{\gamma} = \frac{\mathrm{Ma} H}{\ell_c} \lesssim 1.$$

This capillary number is larger than the standard capillary number (so that the Marangoni effect is larger than the viscous stress induced by the evaporative flow) but is still small, so that the dominant physics in determining the droplet shape remains the bare interfacial tension.

III. MATHEMATICAL MODEL: DERIVATION AND NUMERICAL APPROXIMATION

In this section we give details of the derivation and implementation of the gravito-elasto-capillary model for the shape evolution of the droplets during evaporation. We distinguish two main phases during the evaporation of HFBI droplets:

1. *Before the formation of the elastic, HFBI film.* In this phase the shape of the drop is dominated by the interplay of gravity and capillarity subject to evaporation with a constant contact area. In this phase, the shape of the drop is given by the classical Young–Laplace equation. As water evaporates, the HFBI concentration increases, though in this phase it is not sufficient to trigger the formation of an elastic film at the air–water interface.

2. *After the formation of the HFBI film.* When the concentration of the hydrophobin molecules on the free surface is sufficient, HFBI self-organizes to form a solid film. In this phase, the shape of the drop is dictated by the elasticity of the membrane, the interfacial tension and the gravity acting on the drop.

In all phases, we neglect concentration-dependent variation of the interfacial tension, though this is also possible.

A. Phase 1: Shape determined by gravity and capillarity

In this phase we use the theoretical framework proposed in [17] and expanded in [18]. In particular, we assume axisymmetry and we fix the center of a Cartesian frame (x, y, z) at the apex of the drop. Let $(r(t, S), z(t, S))$ be the curve describing the shape of the droplet, where r is the radial distance from the z axis and S is the arclength of the curve. We denote by $\phi(t, S)$ the local tangent angle, so that

$$\begin{cases} \dfrac{\mathrm{d}r}{\mathrm{d}S} = \cos\phi; \\ \dfrac{\mathrm{d}z}{\mathrm{d}S} = \sin\phi; \end{cases} \tag{S1}$$

Using these variables, we can express the total curvature of the surface as [17]

$$\kappa = \pm\left(\frac{\mathrm{d}\phi}{\mathrm{d}S} + \frac{\sin\phi}{r}\right),$$

the sign in front of the parenthesis is positive if we are considering a sessile droplet (the droplet lies below the curve (r, z)), while it is negative in the case of a pendant droplet (the droplet lies above the curve (r, z)).

Due to the hydrostatic pressure profile within the droplet, the pressure at a position (r, z) can be written

$$p = p_T - \rho g z = \pm\frac{\gamma}{V_i^{1/3}}\alpha - \rho g z$$

where p_T is the pressure at $z = 0$ and $\alpha = \pm V_i^{1/3} p_T/\gamma$ is dimensionless, with a positive or a negative sign depending on whether the droplet is sessile or pendant, respectively. Thus, we can write the Young–Laplace equation as

$$\rho g z - p_T = \pm\gamma\left(\frac{\mathrm{d}\phi}{\mathrm{d}S} + \frac{\sin\phi}{r}\right). \tag{S2}$$

Using $V_i^{1/3}$ as the characteristic length scale of the problem, we introduce the following dimensionless quantities

$$\tilde{r} = \frac{r}{V_i^{1/3}}, \qquad \tilde{z} = \frac{z}{V_i^{1/3}}, \qquad \tilde{S} = \frac{S}{V_i^{1/3}}. \tag{S3}$$

In the following, we drop the tildes from all the dimensionless variables for notational compactness. We can rewrite the set of ODEs (S1)-(S2) in the following dimensionless form

$$\begin{cases} \dfrac{\mathrm{d}r}{\mathrm{d}S} = \cos\phi, \\ \dfrac{\mathrm{d}z}{\mathrm{d}S} = \sin\phi, \\ \dfrac{\mathrm{d}\phi}{\mathrm{d}S} = \mathrm{Bo}\, z - \alpha - \dfrac{\sin\phi}{r}. \end{cases} \tag{S4}$$

To compute the shape of a droplet having a volume $V(t)$, we use the following initial conditions:

$$\begin{cases} r(t, 0) = 0, \\ z(t, 0) = 0, \\ \phi(t, 0) = 0. \end{cases} \tag{S5}$$

The system (S4) is integrated using the software MATHEMATICA iteratively changing the value of α. In particular, we solve the system (S4) until $\phi = -\pi$. Then, we identify the value(s) S_{end} such that

$$r(t, S_{\mathrm{end}}) = r_c, \tag{S6}$$

where r_c is the (dimensionless) radius of the contact surface between the drop and the substrate, which is measured from the experiments. We iterate this process until the volume of the droplet V coincides with the target one $V(t)$.

We observe that the boundary conditions (S5) are not suitable for use in the numerical procedure because of the singularity of the Young–Laplace equation (S2) when $r = 0$. To circumvent this difficulty, we exploit the following series expansion:

$$\begin{cases} r(t, \varepsilon_0) = \varepsilon_0 r_1 + o(\varepsilon_0), \\ z(t, \varepsilon_0) = \varepsilon_0 z_1 + o(\varepsilon_0), \\ \phi(t, \varepsilon_0) = \varepsilon_0 \phi_1 + o(\varepsilon_0). \end{cases} \tag{S7}$$

Plugging (S7) into (S4), we find

$$\begin{cases} r_1 = 1, \\ z_1 = 0, \\ \phi_1 = -\dfrac{\alpha}{2}, \end{cases}$$

so that, in place of (S5), we neglect the remainder in (S7) and we use these expressions as initial conditions in the numerical algorithm, choosing a suitable, small ε_0.

B. Phase 2: Shape determined by gravity, capillarity and elasticity

Following [19], we can rewrite Eq. (3) of the main paper as a system of first order ordinary differential equations. The principal curvatures κ_s and κ_θ can be expressed as [20, 21]

$$\kappa_s = \pm \frac{\mathrm{d}\phi}{\mathrm{d}s}, \qquad \kappa_\theta = \pm \frac{\sin\phi}{r}, \tag{S8}$$

where again we take a plus or a minus if we are considering a sessile or a pendant droplet, respectively.

Recalling that the constitutive equations for the meridional and hoop stresses are

$$\begin{cases} \tau_s = \dfrac{E}{1-\nu^2} \dfrac{1}{\lambda_\theta} \left[(\lambda_s - 1) + \nu(\lambda_\theta - 1) \right] + \gamma, \\ \tau_\theta = \dfrac{E}{1-\nu^2} \dfrac{1}{\lambda_s} \left[(\lambda_\theta - 1) + \nu(\lambda_s - 1) \right] + \gamma, \end{cases} \tag{S9}$$

Eq. (3) of the main paper becomes

$$\begin{cases} \dfrac{\mathrm{d}r}{\mathrm{d}s_0} = \lambda_s \cos\phi, \\ \dfrac{\mathrm{d}z}{\mathrm{d}s_0} = \lambda_s \sin\phi, \\ \dfrac{\mathrm{d}\phi}{\mathrm{d}s_0} = \dfrac{\lambda_s}{\tau_s} \left(\pm(\rho g z - p_T) - \dfrac{\sin\phi}{r}\tau_\theta \right), \\ \dfrac{\mathrm{d}\tau_s}{\mathrm{d}s_0} = \lambda_s \dfrac{\tau_\theta - \tau_s}{r} \cos\phi, \end{cases} \tag{S10}$$

where κ_θ, τ_θ and λ_s can be obtained through (S9), (S8) and the relationships

$$\lambda_s = \frac{\mathrm{d}s}{\mathrm{d}s_0}, \qquad \lambda_\theta = \frac{r}{r_0}. \tag{S11}$$

As done for the drop without the elastic membrane, the system (S10) is non-dimensionalized with respect to the characteristic length $V_i^{1/3}$ and the surface tension γ. We introduce the dimensionless functions (S3) and

$$\tilde{\tau}_s = \frac{\tau_s}{\gamma}, \qquad \tilde{\tau}_\theta = \frac{\tau_\theta}{\gamma}. \tag{S12}$$

In addition to the parameters already discussed, this non-dimensionalization introduces a dimensionless interfacial modulus

$$\mathcal{E} = E/\gamma.$$

For notational convenience, we drop the tildes to denote the dimensionless counterparts of the dimensional functions. The system (S10) in dimensionless form becomes

$$
\begin{cases}
\dfrac{\mathrm{d}r}{\mathrm{d}s_0} = \lambda_s \cos\phi, \\[2mm]
\dfrac{\mathrm{d}z}{\mathrm{d}s_0} = \lambda_s \sin\phi, \\[2mm]
\dfrac{\mathrm{d}\phi}{\mathrm{d}s_0} = \dfrac{\lambda_s}{\tau_s}\left(\mathrm{Bo}\, z - \alpha - \dfrac{\sin\phi}{r}\tau_\theta \right), \\[2mm]
\dfrac{\mathrm{d}\tau_s}{\mathrm{d}s_0} = \lambda_s \dfrac{\tau_\theta - \tau_s}{r}\cos\phi,
\end{cases}
\tag{S13}
$$

which is complemented by the initial conditions

$$
\begin{cases}
r(t,\, 0) = 0, \\
z(t,\, 0) = 0, \\
\phi(t,\, 0) = 0, \\
\tau_s(t,\, 0) = \tau_{s0}.
\end{cases}
\tag{S14}
$$

Finally, the membrane is assumed be constrained so that it is pinned at the contact line, namely

$$r(t,\, L) = r_c, \tag{S15}$$

analogously with (S6).

The system is solved by fixing the value of τ_s and by performing a shooting method until the boundary condition (S15) is satisfied. However, as before, the system is singular at $s = 0$ since r vanishes. Thus, we perform the following series expansion:

$$
\begin{cases}
r(t,\, \varepsilon) = \varepsilon r_1 + \varepsilon^2 r_2 + o(\varepsilon^2), \\
z(t,\, \varepsilon) = \varepsilon z_0 + \varepsilon^2 z_2 + o(\varepsilon^2), \\
\phi(t,\, \varepsilon) = \varepsilon \phi_1 + \varepsilon^2 \phi_2 + o(\varepsilon^2), \\
\tau_s(t,\, \varepsilon) = \tau_{s0} + \varepsilon \tau_{s1} + \varepsilon^2 \tau_{s2} + o(\varepsilon^2),
\end{cases}
\tag{S16}
$$

1. Leading order expansion

Substituting the expansion (S16) into (S13), we find at leading order that

$$
\begin{cases}
r_1 = \dfrac{\mathcal{E}}{(\nu - 1)(\tau_{s0} - 1) + \mathcal{E}}, \\[2mm]
z_1 = 0, \\[2mm]
\phi_1 = -\dfrac{\alpha r_1}{2\tau_{s0}}, \\[2mm]
\tau_{s1} = 0.
\end{cases}
\tag{S17}
$$

Thus, in place of (S14), we neglect the remainder in (S16) and we use these expressions as initial conditions in the numerical algorithm, choosing a suitable, small ε.

2. Higher order terms

Similarly to (S17), we can perform a series expansion of (S13) at higher orders. In particular, second order terms in (S16) read

$$
\begin{cases}
r_2 = 0, \\
z_2 = -\dfrac{\alpha r_1^2}{4\tau_{s0}}, \\
\phi_2 = 0, \\
\tau_{s2} = -\dfrac{(\tau_{s0}-1)(-\nu+2r_1-1)\left(4\frac{\mathrm{d}^3 r_0}{\mathrm{d}s_0^3}(0)\tau_{s0}^2 + \alpha^2 r_1^2\right)}{64(r_1-1)r_1\tau_{s0}^2},
\end{cases}
\tag{S18}
$$

where an expansion up to the third order in r and ϕ is needed to compute τ_{s2}. The quantity $\mathrm{d}^3 r_0/\mathrm{d}s_0^3(0)$ can be computed by expanding (S7) up to the third order in ε_0, obtaining

$$
\frac{\mathrm{d}^3 r_0}{\mathrm{d}s_0^3}(0) = -\frac{\alpha_0^2}{4},
$$

where α_0 is the value of α in the initial configuration of the membrane. For later convenience, we observe that if we similarly expand the hoop tension

$$
\tau_\theta(t,\,\varepsilon) = \tau_{\theta 0} + \varepsilon\tau_{\theta 1} + \varepsilon^2\tau_{\theta 2} + o(\varepsilon^2),
$$

a direct computation shows that

$$
\tau_{\theta 0} = \tau_{s0}, \qquad \tau_{\theta 1} = 0, \qquad \tau_{\theta 2} = 3\tau_{s2}.
\tag{S19}
$$

We remark that, as the meridional tension τ_s in $s=0$ goes to zero, some terms of the series expansion become singular. To avoid this issue, we first assume that $\tau_{s0}=0$ and then we perform the expansion (S16). Specifically, we also get that α (i.e. the dimensionless pressure at the apex of the droplet) is zero. An explicit expansion up to the second order is given by

$$
\begin{cases}
r(t,\,\varepsilon) = \varepsilon r_1 + o(\varepsilon^2) = \dfrac{\mathcal{E}}{-\nu + \mathcal{E} + 1}\varepsilon + o(\varepsilon^2), \\[2mm]
z(t,\,\varepsilon) = \varepsilon^2 z_2 + o(\varepsilon^2) = \pm\dfrac{r_1\sqrt{8\mathrm{Bo}(r_1-1)r_1^3 + \alpha_0^2(-\nu+2r_1-1)}}{4\sqrt{-\nu+2r_1-1}}\varepsilon^2 + o(\varepsilon^2) \\[2mm]
\phi(t,\,\varepsilon) = \dfrac{2(\varepsilon^2 z_2)}{(\varepsilon r_1)} + o(\varepsilon^2), \\[2mm]
\tau_s(t,\,\varepsilon) = \dfrac{\mathrm{Bo}}{8}(\varepsilon r_1)^2 + o(\varepsilon^2).
\end{cases}
$$

Interestingly, the convexity of τ_s in $s_0=0$ depends on the the sign of Bo:

- If Bo is positive, then τ_s is convex and has a local minimum at $s=0$; as a result, the apex of the sessile droplet is the nucleation point of buckling.

- If Bo is negative, then τ_s exhibits a local maximum at $s=0$ and the tension must first become negative for $s>0$, away from the apex. (The membrane must have already buckled in a neighbourhood of $s=0$ when the tension first becomes zero at the apex.)

We note also that, since $\tau_{\theta 2}$ is three times τ_{s2} as shown in (S19), then the hoop stress decreases faster than the meridional stress, even when $\tau_{s0} \neq 0$. Thus, we expect that when compression occurs first away from the drop apex (i.e. when Bo < 0), the first component of the stress to become zero as the droplet evaporates is τ_θ. As a result, radial wrinkles should appear when Bo < 0 while for Bo > 0 bi-directional crumpling should occur (since τ_θ and τ_s vanish simultaneously at the apex).

As a result, Bo $= 0$ is a sharp transition point, where the nature of the membrane buckling changes dramatically. In the following, we detail the numerical algorithms used to explore the two cases, that is Bo > 0 for sessile and Bo < 0 for pendant droplets.

3. Flattening in sessile droplets

For sessile droplets, we find that the hoop and radial stresses vanish at the centre of the droplet. As discussed in the main paper, this leads to a flat region at the centre of the droplet: since both τ_s and τ_θ vanish, locally the HFBI film cannot sustain a pressure difference across the membrane, it must remain flat, and, further, $\alpha = 0$. While τ_s must be continuous at $s_0 = s_f$ to ensure the global balance of the forces acting on the whole flat region, in principle τ_θ can be discontinuous at $s_0 = s_f$. However, since

$$\lim_{s_0 \to s_f^+} \phi(s_0)$$

is, in general, different from zero, we observe that from the third equation of (S13) also τ_θ must vanish as $s_0 \to s_f^+$. Using (S9), we get

$$\lim_{s_0 \to s_f^+} \lambda_s = \lim_{s_0 \to s_f^+} \lambda_\theta = \frac{\mathcal{E}}{\mathcal{E} + 1 - \nu}.$$

From the expression of the stretches (S11) we get

$$r(t, s_f) = \frac{\mathcal{E}}{\mathcal{E} + 1 - \nu} r_0(t, s_f).$$

Summing up, fixing the value s_f, we need to integrate the system (S13) from $s_0 = s_f$ up to $s_0 = L$ using the initial conditions

$$\begin{cases} r(t, s_f) = \dfrac{\mathcal{E}}{\mathcal{E} + 1 - \nu} r_0(t, s_f), \\ z(t, s_f) = 0, \\ \phi(t, s_f) = \phi_f, \\ \tau_s(t, s_f) = 0; \end{cases}$$

Again, these initial conditions are unsuitable to be directly used numerically, since the fourth equation of (S13) has a singularity when $\tau_s = 0$. To circumvent the problem, we exploit the following asymptotic expansion

$$\begin{cases} r(t, s_f) = \dfrac{\mathcal{E}}{\mathcal{E} + 1 - \nu} r_0(t, s_f) + \varepsilon_f r_1 + o(\varepsilon_f), \\ z(t, s_f) = \varepsilon_f z_1 + o(\varepsilon_f), \\ \phi(t, s_f) = \phi_f + \varepsilon_f \phi_1 + o(\varepsilon_f), \\ \tau_s(t, s_f) = \varepsilon_f^2 \tau_{s2} + o(\varepsilon_f^2). \end{cases} \tag{S20}$$

By substituting these expressions into (S13) and performing a Taylor series expansion, one obtains

$$\begin{cases} r_1 = \dfrac{\mathcal{E} \cos \phi_f}{\mathcal{E} + 1 - \nu}, \\[2mm] z_1 = -\dfrac{\mathcal{E} \sin \phi_f}{\mathcal{E} + 1 - \nu}, \\[2mm] \phi_1 = \dfrac{\cot \phi_f \left(\frac{\mathrm{d}r_0}{\mathrm{d}s_0}(s_f) \left(2\frac{\mathrm{d}r_0}{\mathrm{d}s_0}(s_f) + \cos \phi_f \right) - r_0(s_f)\frac{\mathrm{d}^2 r_0}{\mathrm{d}s_0^2}(s_f) - 3\cos^2 \phi_f \right)}{r_0(s_f) \left(3\cos \phi_f - 2\frac{\mathrm{d}r_0}{\mathrm{d}s_0}(s_f) \right)}, \\[4mm] \tau_{s2} = \dfrac{\left((\mathcal{E} - \nu)^2 - 1 \right) \cos \phi_f \left(\cos \phi_f - \frac{\mathrm{d}r_0}{\mathrm{d}s_0}(s_f) \right)}{2\mathcal{E} r_0(s_f)^2}, \end{cases}$$

where the expression of ϕ_1 can be obtained only if we take into account the terms $\varepsilon_f^2 r_2$ and $\varepsilon_f^2 z_2$ in the expansion of r and z (S20), even though we do not report explicitly their expressions.

Summing up, the shape equations (S13) are integrated numerically from $s_0 = s_f + \varepsilon_f$ up to $s_0 = L$, fixing $\alpha = 0$ and by selecting a particular value of s_f. As initial conditions, we use (S20) and perform a shooting method, changing the value of ϕ_f until the boundary condition (S15) is satisfied.
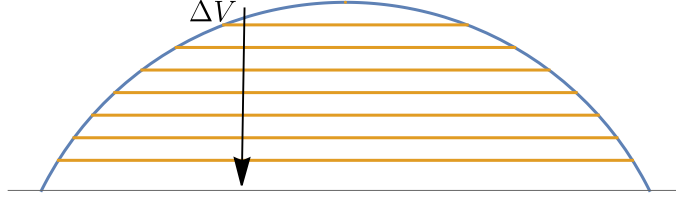
FIG. S4. Representation of the "spherical segment" geometrical approximation, where the flattened droplet is modeled as a spherical segment. As water evaporates we remove a spherical cap from the apex of the droplet whose volume corresponds to the evaporated volume.

a. Spherical segment approximation A simple geometrical model allows us to obtain a very close approximation of the diameter of the flattened region by approximating the droplet shape as a spherical segment in which the radius of curvature of the sphere and the contact line radius are both kept constant, as shown in FIG. S4.

This approximation may be justified by the high energetic cost of changing the Gaussian curvature in regions where the stress is significant — it is energetically cheaper to extend the flat spot radius since the both components of the stress are close to zero here, by assumption.

Given the volume V_f of the droplet at the onset of crumpling and the radius r_c of the contact line, we can compute the height h of the spherical cap using the following formula

$$V_f = \frac{\pi h}{6}(3r_c^2 + h^2).\tag{S21}$$

By applying the Pythagorean theorem, we get

$$R = \frac{h^2 + r_c^2}{2h}.$$

Finally, we can find the evaporated volume $V_f - V$ for a given diameter d of the flattened region by using again the formula for the volume of a spherical cap, as in (S21), obtaining

$$V_f - V = \frac{\pi}{12}\left(2R - \sqrt{4R^2 - d^2}\right)\left(\frac{1}{4}\left(2R - \sqrt{4R^2 - d^2}\right)^2 + \frac{3d^2}{4}\right)$$

and hence

$$\frac{V_f - V}{V_f} = \frac{\pi}{12}\left(\frac{2R}{V_f^{1/3}} - \sqrt{\frac{4R^2 - d^2}{V_f^{2/3}}}\right)\left(\frac{1}{4V_f^{2/3}}\left(2R - \sqrt{4R^2 - d^2}\right)^2 + \frac{3d^2}{4V_f^{2/3}}\right).\tag{S22}$$

The geometrical nature of this relationship suggests that the rescaled flat spot diameter, $d/V_f^{1/3}$, should be a function only of the rescaled volume change, $(V_f - V)/V_f$, as is observed experimentally.

Moreover, and despite the crude nature of this simple approximation, we nevertheless find very good agreement with the experimental results, as shown in FIG. 2 of the main paper.

4. Wrinkling in pendant droplets

In contrast to sessile droplets, we find that in pendant droplets, the hoop stress vanishes *before* the radial stress does. To model wrinkling in pendant droplets we therefore numerically solve (S13) until either we reach $s_0 = L$ or τ_θ becomes zero at $s_a \in (0, L)$. In the latter case we switch to the far from threshold model developed in [19], maintaining $\tau_\theta = 0$ in some wrinkled region. Since $\tau_\theta = 0$ in this region, we get

$$\lambda_\theta = 1 - \frac{1 - \nu^2}{\mathcal{E}}\lambda_s - \nu(\lambda_s - 1),\tag{S23}$$

which is the actual stretch of the wrinkled surface, while the stretch of the axisymmetric pseudosurface is denoted by

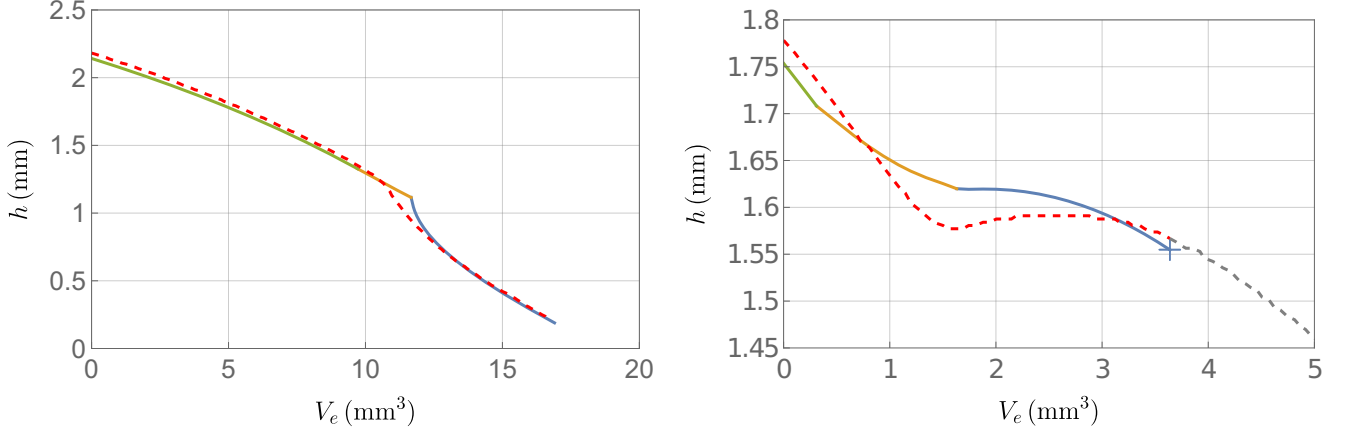$$\widehat{\lambda}_\theta = \frac{r}{r_0}.$$

FIG. S5. Height of the droplet h as a function of the evaporated volume V_e for (left) a sessile droplet with initial volume $V_i = 18.68 \, \text{mm}^3$ and initial concentration $C = 2 \, \mu\text{mol L}^{-1}$ and (right) a pendant droplet with initial volume $V_i = 7.77 \, \text{mm}^3$ and initial concentration $C = 4 \, \mu\text{mol L}^{-1}$. The dashed line is extracted from the experimental data. The experimental curve are plotted in gray at points corresponding to a depinned contact line. The solid curve represents the model prediction. Specifically, the green curve corresponds to Phase 1, where the elastic membrane is not present, the orange curve corresponds to Phase 2 before wrinkling/crumpling, when the HFBI film is formed, and the blue curve indicates that crumples (for the sessile droplet) and wrinkles (in the pendant droplet) are present. The point at which the model predicts the interpenetration of the membrane with the substrate is denoted '+' — simulations cease at this point.

Substituting (S23) into (S9) we get

$$\tau_s = \frac{\mathcal{E}}{\lambda_\theta} \left(\lambda_s - 1 - \frac{\nu}{\mathcal{E}} \lambda_s \right) + 1, \tag{S24}$$

which represents the meridional strain in the wrinkled configuration. The meridional stress $\widehat{\tau}_s$ on the pseudosurface can be computed from (S24) as

$$\widehat{\tau}_s = \frac{\lambda_\theta}{\widehat{\lambda}_\theta} \tau_s.$$

Thus, on the pseudosurface the balance of forces becomes

$$\frac{\mathrm{d}(r\widehat{\tau}_s)}{\mathrm{d}s} = 0,$$

and therefore the system (S13) can be rewritten as

$$\begin{cases} \dfrac{\mathrm{d}r}{\mathrm{d}s_0} = \lambda_s \cos\phi, \\[2mm] \dfrac{\mathrm{d}z}{\mathrm{d}s_0} = \lambda_s \sin\phi, \\[2mm] \dfrac{\mathrm{d}\phi}{\mathrm{d}s_0} = \dfrac{\lambda_s}{\tau_s} \left(\text{Bo} \, z - \alpha \right), \\[2mm] \dfrac{\mathrm{d}\widehat{\tau}_s}{\mathrm{d}s_0} = -\lambda_s \dfrac{\widehat{\tau}_s}{r} \cos\phi. \end{cases} \tag{S25}$$

The system is solved for $s_0 \in [s_a, s_b]$, namely in the interval where

$$\widehat{\lambda}_\theta < 1 - \frac{1 - \nu^2}{\mathcal{E}} \lambda_s - \nu(\lambda_s - 1),$$

while in $[s_b, L]$ we switch back to the membrane model (S13).

In FIG. S5 we show the plots of the height of the droplet as a function of the evaporated volume for both sessile and a pendant droplets. Note that, for pendant droplets, the shape predicted by the model interpenetrates the substrate;
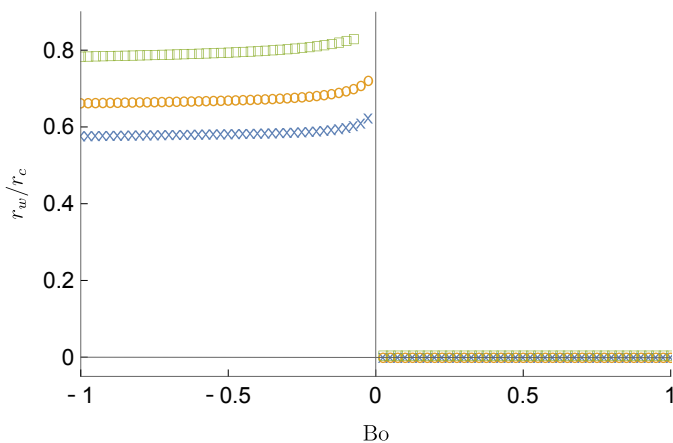
FIG. S6. Plot of the normalized radius r_w/r_c versus Bo. Here, r_w is the radial position where wrinkling/crumpling first appear. In the plots, $V_i = 7.77\,\mathrm{mm}^3$, $C = 4\,\mathrm{\mu mol\,L^{-1}}$, $\gamma = 55\,\mathrm{mN\,m^{-1}}$ while $E = 150, 200, 400\,\mathrm{mN\,m^{-1}}$ (blue crosses, orange circles, and green squares, respectively).

we indicate this point in FIG. S5 with '+' and cease the simulation at this point. Interestingly, however, this point corresponds almost exactly with the point at which the contact line is observed to depin experimentally (indicated by the transition from the red to the gray dashed line in the right-hand plot of FIG. S5). In particular, the "depinning" of the contact line seems to be induced by the contact between the membrane and the substrate. Such an interaction is not modeled in this work and will be studied in a future paper.

FIG. S6 shows how the nucleation point of wrinkles for the pendant drop case (i.e. the first point where τ_θ becomes zero as water evaporates) varies with the two key dimensionless parameters: the ratio $\mathcal{E} = E/\gamma$ and Bo < 0. We note that as $\mathcal{E}$ increases or Bo approaches zero, the nucleation point moves closer to the contact line. This is noteworthy because it emphasizes the discontinuity in behavior that is observed around the zero Bond number limit: as Bond number Bo $\nearrow 0$ the nucleation point moves towards the contact line but for Bo > 0 the nucleation point lies precisely at the center of the droplet.

[1] M. Linder, K. Selber, T. Nakari-Setälä, M. Qiao, M.-R. Kula, and M. Penttilä, Biomacromolecules **2**, 511 (2001).
[2] D. Legland, I. Arganda-Carreras, and P. Andrey, Bioinformatics **32**, 3532–3534 (2016).
[3] O. Krivosheeva, A. Dėdinaitė, M. B. Linder, R. D. Tilton, and P. M. Claesson, Langmuir **29**, 2683 (2013).
[4] G. S. Patience, *Experimental methods and instrumentation for chemical engineers* (Elsevier, 2017).
[5] L. Korson, W. Drost-Hansen, and F. J. Millero, J. Phys. Chem. **73**, 34 (1969).
[6] R. Yamasaki and T. Haruyama, J. Phys. Chem. B **120**, 3699 (2016).
[7] H. H. Al-Terke, *Study of hydrophobin behaviour at air-water interface*, Master's thesis, Aalto Univesity (2017).
[8] A. Paananen, E. Vuorimaa, M. Torkkeli, M. Penttilä, M. Kauranen, O. Ikkala, H. Lemmetyinen, R. Serimaa, and M. B. Linder, Biochemistry **42**, 5253 (2003).
[9] C. Nieto de Castro, S. Li, A. Nagashima, R. Trengove, and W. Wakeham, J. Phys. Chem. Ref. Data **15**, 1073 (1986).
[10] J. R. Welty, C. E. Wicks, G. Rorrer, and R. E. Wilson, *Fundamentals of momentum, heat, and mass transfer* (John Wiley & Sons, 2009).
[11] J. H. Perry, *Perry's Chemical Engineers' Handbook* (ACS Publications, 1950).
[12] G. J. Gittens, J. Colloid. Interf. Sci. **30**, 406 (1969).
[13] R. Piazza, S. Buzzaccaro, and E. Secchi, J. Phys.: Condens. Matter **24**, 284109 (2012).
[14] R. D. Deegan, O. Bakajin, T. F. Dupont, G. Huber, S. R. Nagel, and T. A. Witten, Nature **389**, 827 (1997).
[15] R. Bhardwaj, X. Fang, and D. Attinger, New J. Phys. **11**, 075020 (2009).
[16] W. Ristenpart, P. Kim, C. Domingues, J. Wan, and H. A. Stone, Phys. Rev. Lett. **99**, 234502 (2007).
[17] E. A. Boucher, Rep. Prog. Phys. **43**, 497 (1980).
[18] C. Y. H. Wong, M. Adda-Bedia, and D. Vella, Soft Matter **13**, 5250 (2017).
[19] S. Knoche, D. Vella, E. Aumaitre, P. Degen, H. Rehage, P. Cicuta, and J. Kierfeld, Langmuir **29**, 12463 (2013).
[20] A. Libai and J. G. Simmonds, *The Nonlinear Theory of Elastic Shells* (Cambridge University Press, 1998).
[21] S. Knoche and J. Kierfeld, Physical Review E **84**, 046608 (2011).